communications earth & environment

Article

A Nature Portfolio journal

https://doi.org/10.1038/s43247-025-03157-5

Out-of-season water escape during Mars' northern summer triggered by a strong localized dust storm

Adrián Brines[1,2] ✉, Shohei Aoki[2,3] ✉, Frank Daerden[4], Michael S. Chaffin[5], Samuel A. Atwood[6,7], Susarla Raghuram[5], Bruce A. Cantor[8], Yannick Willame[4], Loïc Trompet[4], Geronimo L. Villanueva[7], Michael J. Wolff[9], Michael D. Smith[7], Christopher S. Edwards[10], Ian R. Thomas[4], Giuliano Liuzzi[11], Lori Neary[4], Manish R. Patel[12], Miguel Angel López-Valverde[1], Armin Kleinböhl[13], Hoor AlMazmi[14], James Whiteway[15], AnnCarine Vandaele[4], Bojan Ristic[4] & Giancarlo Bellucci[16]

Mars almost certainly had a considerable amount of water in its past. Recent observations reveal that during southern summer, when the atmosphere is warmer and dustier, water vapor can reach high altitudes without condensing, leading to water loss to space. Here, by combining infrared, visible, and ultraviolet data from multiple Mars orbiters, we identify a new pathway for water loss, observed for the first time to our knowledge during the opposite season. Our findings show that a strong, localized, and short-lived dust storm in Martian Year 37 (August 2023) drove considerable vertical transport of water vapor in the northern summer season. Just days after the storm, enhanced water vapor concentrations were observed at altitudes over 40 km across northern high latitudes, followed by an increase in escaping hydrogen detected at the exobase. These results suggest that water loss on Mars can be triggered by strong local dust storms at any time of year.

Strong geographical and mineralogical evidence on Mars suggests that liquid water once flowed across its surface[1,2]. Over the past decade, multiple studies analyzing the deuterium-to-hydrogen (D/H) ratio in Martian water reservoirs have revealed an enrichment of deuterium relative to Earth. Since hydrogen (H) atoms escape more easily than deuterium (D) atoms, the D/H ratio serves as a key indicator of water loss to space over the planet's history. Recent estimates place the D/H ratio at ~ 0.001, five to eight times higher than on Earth, suggesting that Mars has lost the equivalent of hundreds of meters of global equivalent water layer (GEL) over the past 4 billion years[3–7]. This substantial water loss has played a major role in shaping Mars' current dry environment.

Like Earth, Mars experiences four seasons due to a similar axial tilt. Superimposed on that, its elliptical orbit creates notable seasonal differences. During northern summers, Mars is farther from the Sun, resulting in colder temperatures and a relatively dust-free atmosphere. In contrast, southern summers are warmer, as they coincide with Mars' closest approach to the Sun, allowing a larger solar flux to reach the planet. The warmer atmosphere causes stronger winds and circulation, and more lifting of dust from the surface, which in turn heats the atmosphere further. Additionally, superimposed to this orbital effect, the Martian climate is strongly affected by the topographic asymmetry of the planet with higher elevations in the southern hemisphere controlling the differences between northern and southern summers[8]. This unique combination of the Martian orbit and its surface dichotomy lead to the formation of regional dust storms each southern summer, which in some cases, can escalate to global dust storms[9–11].

Recent observations from Mars Express and ExoMars Trace Gas Orbiter (TGO) have revealed a striking contrast in water vapor vertical distribution between northern and southern summers[12–15]. During northern

[1]Solar System Department, Instituto de Astorfísica de Andalucía (IAA-CSIC), Granada, Spain. [2]Department of Complexity Science and Engineering, University of Tokyo, Kashiwa, Japan. [3]Department of Geophysics, Graduate School of Science, Tohoku University, Sendai, Japan. [4]Royal Belgian Institute for Space Aeronomy (BIRA-IASB), Brussels, Belgium. [5]Laboratory for Atmospheric and Space Physics (LASP), University of Colorado Boulder, Boulder, CO, USA. [6]University of Maryland Baltimore County, Baltimore, MD, USA. [7]NASA Goddard Space Flight Center, Greenbelt, MD, USA. [8]Malin Space Science Systems, San Diego, CA, USA. [9]Space Science Institute, Boulder, CO, USA. [10]Radiant Center for Remote Sensing, Department of Astronomy and Planetary, Northern Arizona University, Flagstaff, AZ, USA. [11]School of Engineering, Universitá degli Studi della Basilicata, Potenza, Italy. [12]School of Physical Sciences, The Open University, Milton Keynes, UK. [13]Jet Propulsion Laboratory, California Institute of Technology, Pasadena, CA, USA. [14]United Arab Emirates Space Agency, Abu Dhabi, UAE. [15]Centre for Research in Earth and Space Science, York University, Toronto, ON, Canada. [16]Istituto di Astrofisica e Planetologia, Roma, Italy. ✉e-mail: adrianbm@iaa.es; adrianbm@g.ecc.u-tokyo.ac.jp; shohei.aoki@edu.k.u-tokyo.ac.jp

summer, water vapor remains confined below 20 km, as it condenses into ice clouds at these altitudes[16,17]. In contrast, the warmer atmosphere of southern summer prevents condensation at low altitudes, allowing the meridional circulation to transport water vapor above 100 km[14,18,19]. Large dust storms, when present, further enhance this upward transport[18,20,21], which after the photolysis of water vapor, ultimately drives hydrogen escape at the exobase[22,23].

This pattern, characterized by higher hydrogen escape fluxes during southern summer, on the order of $\sim 10^9$ cm^{-2} s^{-1}, repeats annually. As a result, the second half of the Martian year is thought to be the primary driver of H escape, in contrast to the much lower flux of $\sim 10^7$ cm^{-2} s^{-1} typically observed during northern summer[7].

Results

Unexpected water vapor enhancement

Here, we report a newly observed increase in water vapor in the middle atmosphere of Mars during the northern summer of Mars Year (MY) 37 (Fig. 1). The Nadir and Occultation for Mars Discovery (NOMAD) instrument onboard TGO has been continuously monitoring water vapor abundance from the lower troposphere up to the mesopause (0–120 km) since 2018 through solar occultation measurements. These data are unique in revealing the vertical distribution of water vapor in detail[14,18,20,24–26]. We analyzed this dataset (see Methods) and compared vertical profiles of water vapor during the northern summer across different MYs.

Figure 1 -a1 and a2 illustrate the latitudinal variation in the vertical distribution of water vapor volume mixing ratios at the evening terminator, for Solar Longitudes (L_S) between 105° and 130° (late northern summer period) in MYs 35 and 37, respectively. Due to the TGO's orbital geometry, only specific latitudes are sampled at particular local times and seasons. To ensure a meaningful comparison between different MYs, we focused on comparing MY 37 with MY 35, as in both years TGO covers similar sampling patterns in terms of latitude, L_S, and local time. A notably higher abundance of water vapor is observed in the middle atmosphere (up to 80 km) at latitudes poleward of 45°N in MY 37 compared to MY 35. Low water vapor abundances comparable to MY 35 were also seen for MY 36[14,26], and are expected by global climate model (GCM) simulations[27,28], currently able to reproduce the seasonal variability of the observed water vapor vertical distribution fairly well[29,30].

The temporal variation in the vertical distribution of water vapor is shown in Fig. 1-b1 and c1 for the northern and southern hemispheres in MY 35, respectively, while Fig. 1-b2 and c2 illustrate the same for MY 37. These panels highlight the stark contrast between the two MYs, particularly in the northern hemisphere in MY 37 (Fig. 1b2), where a significant water vapor injection of approximately 70 parts per million (ppm) at 60 km is observed at L_S = 111°. In contrast, during the same period in MY 35, water vapor abundances in this hemisphere and at these altitudes do not exceed ~4 ppm. This water vapor enhancement persists, with relatively high abundances of around 10 ppm remaining at 60-80 km altitude for several sols until L_S ~ 117°. All individual profiles of water vapor retrieved above 50°N during L_S=110°-130° are shown in Fig. S1 from the Supplementary Information (SI). Moreover, at this time, the aforementioned MY 37 water increase is observed systematically at all longitudes (Fig. S1, see also Fig. S2 and S3

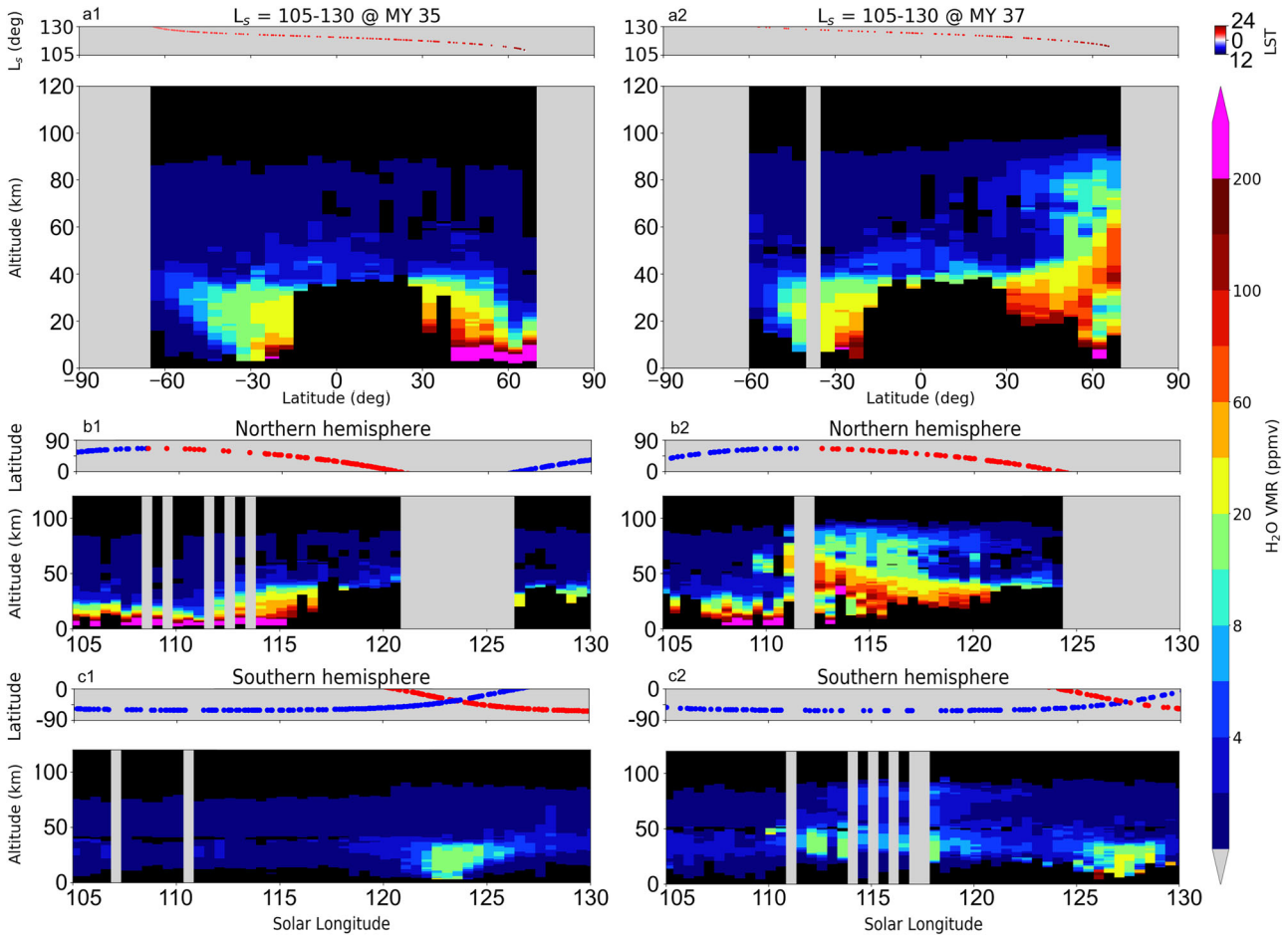

Fig. 1 | Latitudinal and seasonal vertical distribution of water vapor. Vertical distribution of water vapor volume mixing ratio (VMR) as a function of latitude (**a1**, **a2**) and solar longitude for the northern (**b1**,**b2**) and southern (**c1**,**c2**) hemispheres during MYs 35 (left) and MY 37 (right). Dots over each panel indicate the solar longitude, latitude and local time of the NOMAD observations. Blue and red dots indicate morning and evening observations, respectively.

bottom panels), suggesting a quick zonal transport distributing water vapor globally at latitudes poleward of 50°N. After this period beyond L_S=120°, the water vapor distribution in MY 37 returns to patterns similar to those observed in previous years, with the majority of water vapor confined to altitudes below 30 km as shown in Fig. 1b2.

Moreover, the Emirates Mars Ultraviolet Spectrometer (EMUS) onboard the Emirates Mars Mission (EMM) detected a significant increase in hydrogen density at the exobase of about 2×10^5 cm^{-3} (Fig. 2). This value is comparable to the densities observed during late-season regional dust storms (C-storms) towards the end of the dusty season[9], indicated in Fig. 2 with the green shaded area. This density increase is accompanied by a larger hydrogen escape flux of about 5×10^8 cm^{-2}s^{-1}, representing an increase of about 2.5 times relative to the escape observed in the previous year during the same season. The values for the H escape during the aphelion of MY 36 are consistent with those reported in previous analyses[31–33] and close to the value expected from diffusion-limited escape processes[34,35]. However, discrepancies with[36] arise, likely due to assumptions in the retrieval and the locations where the data were gathered.[36] use climatological temperatures in combination with an assumed response of local H density to local temperature to correct their nadir measurements to the global escape rate. In contrast, our EMM/EMUS retrieval approach simultaneously constrains H density and temperature from Ly-α and Ly-β brightness (with Ly-β providing reduced sensitivity to radiative transfer effects), and derives a global escape rate from full phase-angle coverage.

The C storm in MY 36 occurred during L_S=308°–320°[37], which is close to the perihelion season (Ls = 251°), when the solar flux reaching the planet is significantly higher than during the aphelion season, when the MY 37 event occurred. As a result, the temperature at the exobase, which drives the thermal escape of hydrogen[7], is expected to be lower during the aphelion of MY 37 than during the perihelion of MY 36. Even though the hydrogen densities are comparable between these two periods, this could explain the observed two times lower escape rates at Ls = 110° in MY 37 compared to those at Ls = 300° in MY 36 in the third row of Fig. 2.

In addition to the dust storm-driven increase in H escape in MY 37 at $L_S \sim 110°$, the total H loss during the beginning of this year ($L_S = 30° - 100°$) was larger than that estimated for the aphelion of MY 36. The magnitude of escape fluxes is expected to be controlled by the replenishment of hydrogen from the lower atmosphere[7,22]. However, when estimating the H loss rate, parameters other than H density play a key role, such as exospheric temperatures. Since both the water vapor in the middle atmosphere and the H density at the exobase are similar in the beginning of both MYs 36 and 37 (Fig. 2), the observed interannual variation in the H loss rate during this period is likely due to a progressive increase in solar flux during MY 37, as the Solar Cycle reached its maximum in 2023-2024, leading to higher atmospheric temperatures. H escape is more sensitive to changes in temperature than to changes in H density (ref. 7, see their Materials and Methods section), hence, although there is a notable increase in H density due to the dust storm at $L_S \sim 110°$ compared to MY 36, its effect on the H loss rate is moderate relative to the elevated background levels during MY 37.

Although being only a factor 4–6 smaller than the fluxes observed during the perihelion season, the main factor that could lessen the effect of this event on the annual budget of hydrogen loss is its short duration compared to the escape during the second half of the year. The aforementioned escape increase occurs several degrees in L_S after the observed water vapor enhancement in the middle atmosphere (Fig. 2). The observed time lag of approximately one week aligns with the expected hydrogen transport timescale via photochemical processes[22,38,39].

Martian year 37 dust event

What triggered this unusual vertical transport of water vapor? A combination of observations from different space instrumentation provides the answer. We identified a strong, localized dust storm in the northern hemisphere that coincided in time with the water vapor enhancement. The Emirates Mars Infrared Spectrometer (EMIRS) onboard EMM detected a rapid increase in dust opacity between 30°–60° latitude in the northern hemisphere and 0°–60° east longitude at L_S = 108°–111° (Fig. 3a2). This observation is corroborated by nadir measurements of dust opacity from the NOMAD UV-Visible channel (UVIS) (top panel of Fig. 4). Moreover, visible images taken by the MARs Color Imager (MARCI) on Mars Reconnaissance Orbiter (MRO) show how this dust event arose from or around the Antoniadi crater north-west of Syrtis Major (bottom panels of Fig. 4). Atmospheric temperatures retrieved by EMM/EMIRS (see

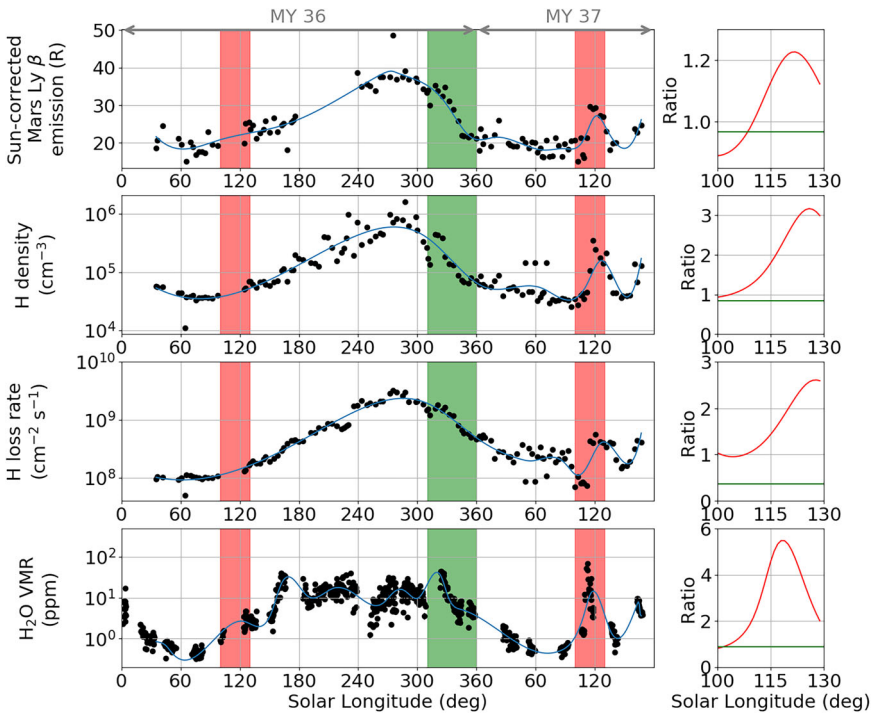

Fig. 2 | Seasonal variation of H density and H escape at the exobase. Seasonal variation of (first row) the average Mars Ly β brightness, (second row) hydrogen density, (third row) derived hydrogen escape rate as observed by EMM/EMUS and (bottom) water vapor VMR retrieved by NOMAD at 60 km at latitudes above 50°N during MYs 36 and 37. Both the hydrogen density and loss rate are the ones at the exobase. The Mars Ly β emission has been corrected for the solar illumination as inferred from MAVEN/EUVM so that time periods with illumination differences due to solar rotation and the solar cycle can be directly compared. The increase in sun-corrected Ly β brightness at $L_S \sim 100°$ in MY 37 following the dust event is a model-independent indicator of an increase in the abundance/temperature of hydrogen in the Mars upper atmosphere, indicating enhanced H escape at this time. The solid lines show the smoothing of the data. The shaded areas indicate (red) the period where the water vapor increase is observed in MY 37 at L_S=105°-130°, and (green) the end of the year C-storm season. For each magnitude, the right hand side panels show the ratio of the values within the shaded areas between MYs 36 and 37. The red line indicates the ratio during the same period in both MYs (red shaded areas), whereas the green line indicates the ratio between the peak within the red shaded area in M 37 and the mean value within the green area.

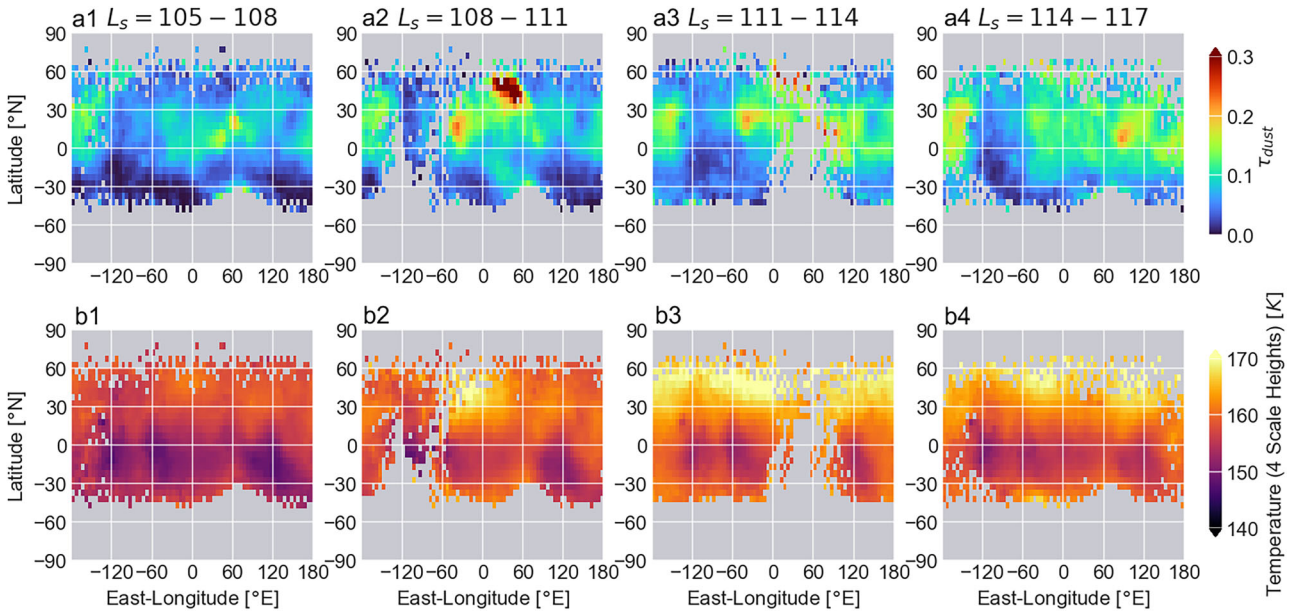

Fig. 3 | Column integrated dust optical depth and temperature. Geographical distribution of column integrated dust optical depth (top panels) and temperature (bottom panels) as observed by EMM/EMIRS from L_S= 105° to 117° in MY 37 (averaged over 3° of L_S). Dust optical depth shows the column measured in the vertical region from the surface up to 4 scale heights (from 0 to ~ 40 km altitude). Temperature corresponds to measurements at roughly 40 km altitude.

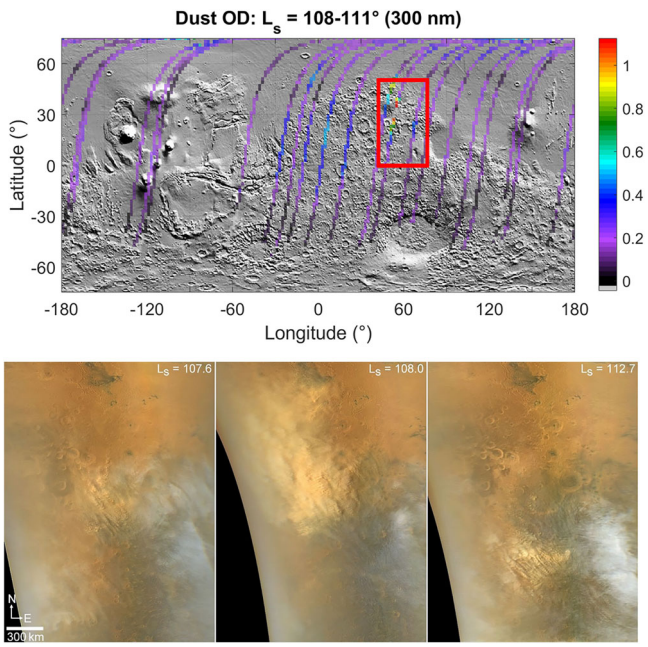

Fig. 4 | UV and visible images of the MY 37 aphelion local dust storm. Geographical distribution of the dust optical depth (300 nm) retrieved from NOMAD/UVIS nadir measurements between L_S=108°-111° of MY37 (using a 2° × 2° averaging grid). (Bottom) MRO-MARCI daily global map images of the early growth of a once in a Martian decade regional dust storm in northwest Syrtis Major (red box in top panel) observed on (left) 21 August 2023 at L_S = 107.6°, (center) August 2023 at L_S = 108.0°, reaching an areal extent of 1.2 × 10^6 km^2. The regional storm persisted for 5-sols. A more common local storm followed, (right) originating in western Syrtis Major on 1 September 2023 at L_S = 112.7°. White features are water ice clouds, dust storms appear as yellowish-orange clouds. Note the water ice clouds above the eastern side of the two storms on the first sol of each event. Color composite created from (437, 546, and 604 nm) filter images and have been cylindrically projected from 0°-40°N, 45°-75°E, at 1 km $pixel^{-1}$.

Methods) showed a rapid global increase of 15 K at an altitude of 4 scale heights (~ 40 km) (Fig. 3b2). The onset of this increase in temperature coincides in time with the dust event and is observed close to the region where the storm is initially detected. This global increase acts as an indicator of warming the lower-to-middle atmosphere and suggests that it is caused by an increase in atmospheric dust, originating from the localized regional dust storm and consequently transported across the planet. The increased temperatures at 4 scale heights (~ 40 km) observed by EMM/EMIRS imply transport of fine dust across the planet at these altitudes, enough to significantly warm the middle atmosphere without substantially increasing the total dust column outside the immediate region of the dust event.

Limb observations from the Mars Climate Sounder (MCS) onboard MRO provided global vertical distributions of dust and water ice cloud extinction, and temperature during this event (Fig. 5; Fig. S2; Fig. S3; Fig. S4). Between L_S=108°-111°, dust concentrations increased significantly in the lower-to-middle atmosphere (within 50° latitude) at altitudes of 20–40 km, causing a temperature rise of approximately 10 K. A decrease in water ice concentration is also observed, which can be explained by the higher saturation vapor pressure caused by the higher temperatures. From then until L_S = 117°, the dust continued to accumulate between 20–40 km at high northern latitudes, as well as below 20 km at mid-low southern latitudes. The radiative heating induced by the dust further increased temperatures by more than 15 K at altitudes of 30–60 km, across a broad latitudinal range from 50°S to 80°N (Fig. 5), consistent with the EMIRS measurements. This temperature increase is also confirmed by CO_2 density analysis from NOMAD measurements (Fig. S5). These temperature changes led to a decrease in water ice cloud content at altitudes of 20–40 km and the formation of a water ice cloud layer above 40 km, similar to the patterns observed in the southern summer season during MY 34's Global Dust Storm (GDS,[40–42]). This is corroborated by MARCI VIS blue channel images at the time of the storm, sensitive to water ice in the atmosphere, that reveal themselves surprisingly bright, indicating water ice was mixed in with the dust at the top of the storm, or above it (Fig. 4).

Water vapor retrievals from NOMAD data show that the sudden, strong increase in water vapor at altitudes above 15 km immediately followed this dust event (bottom panel of Fig. 5 and Fig. S2). NOMAD water vapor retrievals from previous years do not show such an increase at this time of year (Fig. 1 for MY 35 and[14,26] for MY 36). This provides evidence

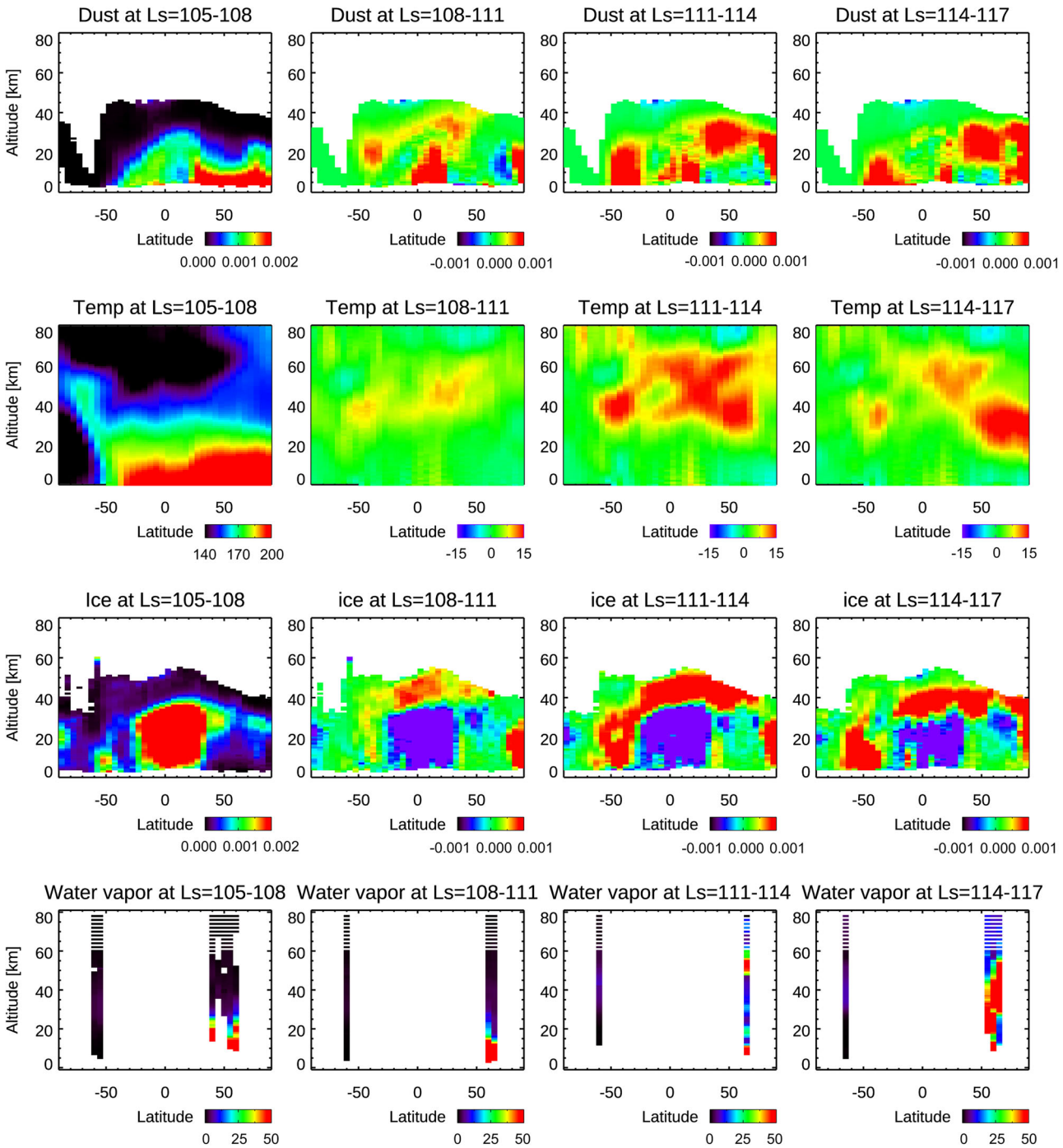

Fig. 5 | Aerosol extinction and temperature during MY 37's local dust storm. Latitudinal distribution of dust extinction [1/km] (top), temperature [K] (second row), water ice extinction [1/km] (third row) as measured by MCS, and water vapor volume mixing ratio [ppmv] (bottom) as measured by NOMAD, from L_S=105° to L_S=117°. Each panel shows the distribution within L_S periods of 3°. For MCS results (three top rows), the first period L_S=105°-108° (first column) shows absolute values, whereas the rest of the periods (second, third and fourth columns) show differences with respect to the first one. Bottom panels show absolute water vapor abundances in all columns. NOMAD and MCS vertical profiles have been averaged within bins of 5° latitude. The reference wavelength for the dust and water ice extinctions are 461 cm^{-1} and 843 cm^{-1}, respectively.

that the exceptional increase in water vapor in the middle atmosphere in northern summer is a direct result of the dust storm during MY 37 and its subsequent atmospheric heating, reducing cloud formation at low altitudes. A schematic representation of this event is illustrated in Fig. 6.

Although the major effects of the storm on water vapor are observed in the northern hemisphere, its impact is also noticeable in other regions of the planet. As shown in Fig. 1c1 and -c2, another enhancement in water vapor abundances between 20–50 km altitude is observed in the southern hemisphere, coinciding in time with the northern hemisphere's dust injection. This southern hemisphere increase of approximately 10–20 ppm was captured by NOMAD during morning terminator observations, as opposed to the evening observations that recorded the northern event. Despite these observational limitations, the increase in water vapor in the southern hemisphere is likely due to the enhanced global circulation driven by the temperature increase and the additional water vapor injected into

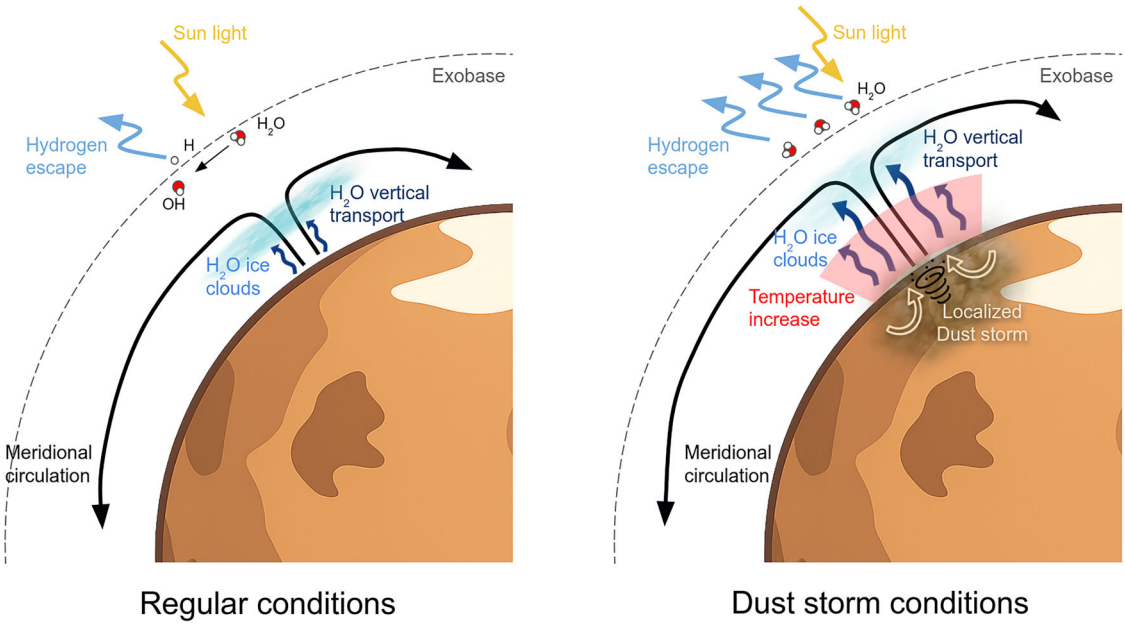

Fig. 6 | Effects of the MY 37 aphelion regional dust storm. Schematic illustrating the atmospheric response to a localized dust storm in the northern hemisphere during the local summer season. High dust loadings significantly increase the absorption of solar radiation, leading to enhanced atmospheric heating, particularly in the middle atmosphere. This thermal response in turn affects the water ice cloud deck, which becomes more vertically extended and less opaque due to reduced water vapor condensation. Additionally, the enhanced atmospheric circulation associated with the dust storm strengthens vertical transport of water vapor from the lower atmosphere, favoring the injection of water to higher altitudes and enhancing the hydrogen escape at the exobase.

the northern hemisphere near the upwelling branches of the Hadley cells (Fig. S6).

The behavior of temperature, dust and water ice observed by MCS in MY 37 early summer (L_S=90°-120°), was never before observed at this season since the start of the MCS observations in MY 28. Although some dust storm events can occur during the northern spring, including a recent dust storm during L_S ~ 40° in MY 35[43], the northern summer season is particularly calm in terms of dust events[44] and no comparable dust activity was seen at this time (after L_S=90°) and location in images by the Mars Orbiter Camera (MOC) on Mars Global Surveyor (MGS) taken between MY 24 and 28. Additionally, the amount of water vapor available in the atmosphere at this moment of the year is significantly larger than that during the spring season[45,46]. This makes the MY 37 regional dust storm unique in 14 MY (about 24.4 Earth years) of orbital remote sensing.

Discussion

Although during northern summer the Mars' atmosphere reaches a minimum dust opacity level of about 0.2-0.5 optical depth[47–49], exceptions occur around the north polar cap and later in the season around the north polar hood[50–52], or at lower latitudes when localized, intense storms form[50,53,54]. As suggested by the simulations of[55], these storms can rapidly inject dust into the atmosphere, reaching altitudes of 30–50 km, coining the name "rocket dust storms". The process is somewhat similar to deep convective cumulonimbus clouds on Earth. However, unlike Earth's storms, which are driven by latent heat release, Mars' rocket dust storms are fueled by solar absorption by dust particles[56].

Such rocket dust storms are expected to be particularly intense during the northern summer season (from late northern winter to late northern summer) in cases when the contrast between the background dust opacity and the storm's opacity is largest. This leads to stronger temperature gradients and more intense vertical winds that sustain the storm[55]. In MY 27, a rocket dust storm was observed in the equatorial region (around 3°S, 24.7°E) at L_S = 135°[54]. Given the location, season, and duration of the explosive dust event in MY 37, we attribute it to being similar to the rocket dust storm observed in MY 27. Further detailed modeling simulations should be done to better understand how this particular storm developed.

How do the effects of this storm compare with global and regional dust storm-induced H escape? Regardless of the exact mechanism by which this storm developed, the overall pattern of high-altitude water vapor increase in the event presented here, is similar to that observed during global and regional dust storms in the southern summer season. Once a significant amount of dust is introduced into the atmosphere, it will ascend to higher altitudes by the meridional circulation (see Fig. S6). The heating of the atmosphere by the dust also leads to an increase in water vapor saturation pressure, and hence to a reduction of water ice cloud formation. This in turn favors transport of water vapor to the middle atmosphere, as demonstrated in ref. 39 for the MY 34 GDS.

Finally, as photolysis rates of H_2O peak in the middle atmosphere[22,27,57], this leads to the increased production of atomic hydrogen. This mechanism, first identified as a driver of the hydrogen escape response to high-altitude water vapor by ref. 38, has since been further investigated in models.[58] quantified the contributions of different altitudes to the exospheric hydrogen budget, highlighting the 60 km region as a key source of hydrogen transported to the upper atmosphere. Together, these processes explain the observations of atomic hydrogen in the upper atmosphere by EMUS (Fig. 2), following the observed increase of water vapor in the middle atmosphere by NOMAD illustrated in Fig. 1 and bottom panel of Fig. 2.

It is important to note that this event in MY 37 is exceptional in that it produced a clear increase in water vapor abundances in the middle atmosphere, reaching values close to those observed during the C-storm period in MY 36 at high northern latitudes (bottom row of Fig. 2). Hydrogen densities at the exobase were also similar between these two periods (first and second rows of Fig. 2). Such conditions of enhanced water vapor and exospheric H density are rarely observed outside the perihelion dusty season, and this represents the first example of an event where dust activity is seen to impact H loss outside of southern summer. The magnitude of the H loss rate, however, seems to be at least a factor 2 lower than the mean H escape observed during the C-storm period of MY 36, as shown in Fig. 2. Nevertheless, the MY 37 dust storm driven H escape presented here is comparable to the values reported by ref. 22 during previous C-storm periods close to 3×10^8 cm^{-2} s^{-1} escape rates. Notice however that some model-based studies report larger escape rates close to 10^9 cm^{-2} s^{-1} during C-storm periods[58,59].

Based on our results and these references, besides some discrepancies, a hierarchy could be established regarding the impact of lower atmospheric effects on the H escape: the perihelion dusty season being the most relevant[22,58], followed by global dust storms, and finally type C and regional storms such as the one studied here.

What are the implications for the understating of water loss? From current water isotopic fractionation measurements, a 137 m deep GEL is expected to have been lost into space throughout recent Martian history[4,5]. To reach this estimate, a global planet-wide average escape rate to space of 4.9×10^9 molecules cm^{-2} s^{-1} would be needed[60]. However, GCM simulations and observations do not reach this value, and approach it only occasionally during global dust storms. Hence, additional present or/and past hydrogen escape mechanisms are needed to reconcile these results. A key aspect of the reported water escape event is that it was triggered by a strong local dust storm. This study demonstrates that localized dust storms, even during the aphelion season, can trigger the transport of water vapor to high altitudes and enhance hydrogen escape. However, unlike the perihelion dust season, which occurs annually and sustains larger and longer escape rates, northern summer regional storms appear to be much rarer, with only two such cases observed in the past ten MY (including this event and another in MY27;[55]). With current and future instrumentation systematically sounding Mars, it will be possible to confirm or refine these statistics. While their long-term contribution to Mars' water loss budget is limited, these events remain important as they reveal an additional, if infrequent, pathway for atmospheric escape.

Could these strong northern summer storms affect the global budget of hydrogen lost to space? With Mars' present-day obliquity, the hydrogen escape rates during the aphelion and perihelion seasons are orders of magnitude apart[38,60,61], with the perihelion season, particularly during southern summer, driving the bulk of the escape. The anomalous aphelion escape enhancement induced by the MY 37 dust storm, while presenting a strong contrast to the expected escape during this season, is still far from the typical perihelion escape rates, both due to 1) the difference in maximum escape rates and 2) the short duration of the MY 37 storm compared to the whole dusty season, limiting the ability of this single event to make up for the seasonal discrepancy in escape. Moreover, unlike the perihelion dusty season, such aphelion dust events do not occur every MY and appear to be less frequent than global dust storms typically occurring every four MYs, further constraining their overall impact on long-term hydrogen escape. In addition, Mars' current axial tilt, orbital eccentricity and argument of perihelion make the incident solar flux less intense during northern summer, so that hydrogen reaching the upper atmosphere is less prone to escape. However, the orbital configuration of Mars has not always been as it is today.

Mars' obliquity varies significantly over time due to gravitational interactions with the Sun and other planets (in contrast to Earth, whose Moon stabilizes its axial tilt). As it is one of the main triggers of dust storms, surface winds and their associated dust lifting have a strong dependency on Martian obliquity. At higher obliquities, near-surface winds and dust lifting were possibly more intense[62]. This could have favored the formation of large dust storms more frequently, contributing to larger water loss rates. However, it remains uncertain whether the results for seasonal dust activity was actually more or less intense during periods of high obliquity in Mars' past[63].

Recent studies based on GCM simulations reveal that when increasing the obliquity by 5° (from 25° to 30°), the hydrogen escape rate during the perihelion increases by one order of magnitude[63]. This same study shows that even a higher obliquity of 35° completely changes the seasonal cycle of hydrogen escape, increasing the escape rates by more than three orders of magnitude during aphelion and perihelion. At these high obliquities, with such a large background hydrogen escape, dust storms during the northern summer could have been extremely significant for the total hydrogen escape budget.

Regardless of uncertainties about past climates, this MY 37 northern dust summer dust event reveals that even during low-obliquity periods like that on present-day Mars, when dust is expected to be more settled, a strong localized regional storm can still induce significant water escape.

Methods

Water vapor retrieval scheme

The water vapor profiles presented in this work are obtained from level 1.0 NOMAD SO infrared transmittances, following a two stages retrieval scheme. This methodology has been tested in previous studies and is fully described in refs. 18,25. Here we present a brief summary highlighting the most relevant processing steps.

First, a pre-processing of the NOMAD data is required in order to remove systematic bendings and shifts in the spectral features and to characterize the instrumental noise. Second, a state-of-the-art retrieval control program (RCP) which incorporates the line-by-line and layer-by-layer Karlsruhe Optimized and Precise Radiative Transfer Algorithm (KOPRA,[64]) is used to invert the water vapor vertical profiles. The RCP processor relies on multiparameter nonlinear least squares fitting of measured and modeled spectra[65]. Further information about RCP can be found in ref. 66 and in ref. 67. We perform the inversion of the NOMAD data available from five different diffraction orders: 134 (3011–3035 cm^{-1}), 135 (3034–3058 cm^{-1}), 136 (3056–3081 cm^{-1}), 168 (3775–3805 cm^{-1}) and 169 (3798–3828 cm^{-1}). The first three contain relatively weak absorption lines ($S \sim 10^{-21}$ cm^{-1}/(molecule cm^{-2})), whereas the others show much stronger lines ($S \sim 10^{-19}$ cm^{-1}/(molecule cm^{-2})) from the spectral region close to the ν_3 fundamental band which saturate at low altitudes. The effect of saturation in absorption lines introduces uncertainties and instability in the retrievals. In order to minimize this issue, we only use measurements obtained in optically thin conditions. This way we differentiate between diffraction orders at high tangent altitudes (with strong lines) and at low tangent altitudes (with weak lines) combining up to five different pairs of orders, 134, 135 or 136 with 168 or 169. Typically, we use low altitude orders (134/135/136) below 60 km and high altitude orders (168/169) above 60 km. This transition altitude is not fixed and it is fine tuned for each occultation analyzing the equivalent width W_λ of the strongest lines in the spectral region between 3770-3830 cm^{-1} (ν_3 band), as described in ref. 26. With this technique, RCP performs an elegant combination (global inversion) of the information content in both diffraction orders.

As in previous studies[18,25,26], we use pressure and temperature profiles from specific simulations of the Mars Planetary Climate Model (MPCM;[68]) to define the a priori atmospheric state during the inversion. These simulations are matched to the exact time and location at 50 km altitude of each solar occultation provided by the NOMAD telemetry. They incorporate the latest implementations of the dust and water cycles described in ref. 28 with a comprehensive photochemical scheme from[69] covering all atmospheric layers from the surface to the exobase. The MPCM simulations use the most accurate estimates of dust optical depth available for each Martian Year (MY), based on[11]. To prevent non-physical oscillations in the retrieved profiles, we apply first-order Tikhonov regularization, optimized for each diffraction order looking for a tradeoff between error propagation, vertical resolution, and convergence rate. More details on retrieval sensitivity tests and performance as well as comparison and validation exercises between NOMAD water vapor retrievals from[14] and[17] can be found in refs. 18,25. These exercises revealed an excellent agreement between the different teams regardless the retrieval methodology used to obtain NOMAD water vapor vertical profiles.

Retrieval of hydrogen density and loss rate

Temporal variation of the Lyman beta (Lyβ) line at 102.6 nm, which is a proxy for Mars hydrogen escape, is measured by the Emirates Mars Ultraviolet Spectrometer (EMUS)[70] onboard Emirates Mars Mission (EMM)[71,72]. Compared to the stronger Lyman alpha (Lyα) line, analysis of the weaker Lyβ line is more straightforward because the line is closer to being optically thin, and its brightness is closer to being directly proportional to the column density of the hydrogen atom than Lyα. We present the average Lyβ brightness observed by EMUS over the course of a complete spacecraft orbit for pointing altitudes greater than 500 km, representing the average brightness of the hydrogen corona as a function of time. The observed brightnesses are converted into retrieved parameters for the

hydrogen corona using a data analysis process described in ref. 33 which was extended to retrieve values from Lyα and Lyβ simultaneously using the well-known cross sections of these emission lines. We retrieve three parameters: H density and temperature at 200 km (the nominal exobase altitude), and a Lyα model scale factor used to account for a well-characterized degradation of the EMUS instrument sensitivity at Lyα as a function of time. Together, the retrieved H density and temperature are used to derive the thermal H escape rate to space, assuming that the velocity at the exobase follows a Maxwellain distribution. Retrieved densities and escape rates are presented in Fig. 2. As explained in ref. 33, the uncertainty in the retrieved escape rate is smaller than the uncertainty in both the H exobase density and temperature, because the coronal brightness observed and the escape rate derived have a similar functional dependence on the exobase H parameters. All retrieved values are available on the EMM Science Data Center website.

EMM/EMIRS retrieval of column integrated dust optical depth and temperature

The atmospheric temperatures and dust optical depths derived from EMIRS observations use a constrained linear inversion algorithm originally developed for TES[45,73], with additional updates for EMIRS[74,75]. The retrieval utilizes a forward radiative transfer model that includes multiple scattering by aerosol particles. Surface and atmospheric temperatures are first retrieved from the CO_2 band centered at 667 cm^{-1}. Dust optical depths are then obtained as part of the aerosol retrieval using spectral regions between 100 and 1315 cm^{-1} (excluding the CO_2 band). Surface pressure is obtained from the Mars Climate Database. The model employs aerosol optical properties with an assumed dust effective radius of 1.5 µm, following established approaches for Martian atmospheric studies[76]. Dust is assumed to follow a Conrath vertical profile that varies seasonally and latitudinally[77]. A smoothness constraint is applied to the temperature profile retrieval using a two-point correlation matrix with a correlation length of 0.75 scale heights[73]. Uncertainties in retrieved atmospheric temperature are typically around 2 K in the middle atmosphere, with slightly higher values at the higher altitudes shown here. The estimated uncertainty in dust optical depth for all retrievals shown here is less than 0.05, with most individual values in the 0.01–0.03 range. Further details on the processing and retrieval algorithm for EMM/EMIRS data can be found in ref. 74.

NOMAD UVIS dust retrieval

The retrieval procedure to obtain dust opacities from NOMAD/UVIS nadir measurements is based on the same scheme used for the retrieval of clouds, dust and ozone abundances from SPICAM/UV spectra[78]. It combines the use LIDORT (Linearized Discrete Ordinate Radiative Transfer)[79,80] to perform the radiative transfer calculation, the Mars Climate Database[68] that provides the a priori atmosphere and the Optimal Estimation Method[81] for the inversion. The procedure has been updated to include recent dust[82], ice clouds and surface reflectance models[83]. The method takes advantage of the fact that ice clouds appear bright in the UV compared to the "dark" dust or surface to perform the retrieval. However, bright surface features like ice caps can mimic these features, so regions expected to contain ice are excluded. Further details on this retrieval scheme can be found in ref. 78.

NOMAD SO CO_2 and temperature retrieval

The NOMAD CO_2 densities and temperatures presented in this study have been obtained by performing retrievals of SO measurements from diffraction orders 132 (2966–2990 cm-1) below around 50 km and 148 (3326–3352 cm^{-1}) above around 50 km. The CO_2 lines in the former order appear below 50 km while those of the latter appear below 100 km and saturate below 50 km. The retrieval process is divided into three primary stages. First, the Atmospheric Spectra Inversion Modular Utility Tools (ASIMUT) program is used to determine the total CO_2 column densities along the line of sight for each spectrum. Next, these slant column density profiles are converted into vertical profiles of local number densities using an approach similar to that of[84]. Finally, temperature profiles are calculated based on the hydrostatic equilibrium equation. Once this sequence is complete, the algorithm returns to the initial step, using the updated temperature profile. Several iterations are performed to ensure convergence and to improve the reliability of the retrieved values. For both orders, only a few iterations are required as the CO_2 lines are very weakly dependent on the temperature. Further details on the retrieval of atmospheric temperatures from NOMAD SO observations can be found in[85].

MCS temperature, dust and water ice

The Mars Climate Sounder[86] is a passive infrared radiometer onboard Mars Reconnaissance Orbiter (MRO). It has 5 mid-IR, 3 far IR, and one broadband visible/near-IR channels, which view the atmosphere and surface in limb, nadir, and off-nadir geometries. Each spectral channel uses a linear detector array, which provides an instantaneous radiance profile when pointed at the Mars limb. From the measured radiance profiles, vertical profiles of atmospheric temperature, dust extinction and water ice extinction are retrieved in an altitude range between the surface and 80–90 km with ~5 km vertical resolution[87]. The retrievals used for this work utilize a combination of mid-IR and far IR channels that enables aerosol profile retrievals from limb measurements that reach deeper into the atmosphere than would be possible using mid-IR channels only and allow the derivation of aerosol column optical depths through vertical integration[88].

Data availability

The results retrieved from the Trace Gas Obiter (TGO) NOMAD measurements presented in this work as well as those from the Emirates Mars Mission (EMM) EMIRS and from the Mars Reconnaissence (MRO) MCS, are being archived and available at[89]. The dataset can be accessed directly through the following link: https://doi.org/10.5281/zenodo.17797042.

Received: 2 October 2025; Accepted: 19 December 2025;
Published online: 02 February 2026

References

1. Carr, M. H. & Head III, J. W. Oceans on Mars: an assessment of the observational evidence and possible fate. *J. Geophys. Res. Planets* **108**, 1963 (2003).
2. Jakosky, B. M. et al. Mars' atmospheric history derived from upper-atmosphere measurements of 38Ar/36Ar. *Science* **355**, 1408–1410 (2017).
3. Owen, T., Maillard, J. P., De Bergh, C. & Lutz, B. L. Deuterium on Mars: the abundance of HDO and the value of D/H. *Science* **240**, 1767–1767 (1988).
4. Villanueva, G. et al. Strong water isotopic anomalies in the Martian atmosphere: probing current and ancient reservoirs. *Science* **348**, 218–221 (2015).
5. Villanueva, G. L. et al. Water heavily fractionated as it ascends on Mars as revealed by ExoMars/NOMAD. *Sci. Adv.* **7**, eabc8843 (2021).
6. Aoki, S. et al. Seasonal variation of the HDO/H2O ratio in the atmosphere of Mars at the middle of northern spring and beginning of northern summer. *Icarus* **260**, 7–22 (2015).
7. Clarke, J. T. et al. Martian atmospheric hydrogen and deuterium: seasonal changes and paradigm for escape to space. *Sci. Adv.* **10**, eadm7499 (2024).
8. Richardson, M. I. & Wilson, R. J. A topographically forced asymmetry in the Martian circulation and climate. *Nature* **416**, 298–301 (2002).
9. Kass, D., Kleinböhl, A., McCleese, D., Schofield, J. & Smith, M. Interannual similarity in the Martian atmosphere during the dust storm season. *Geophys. Res. Lett.* **43**, 6111–6118 (2016).
10. Montabone, L. et al. Eight-year climatology of dust optical depth on Mars. *Icarus* **251**, 65–95 (2015).
11. Montabone, L. et al. Martian year 34 column dust climatology from Mars climate sounder observations: reconstructed maps and model simulations. *J. Geophys. Res. Planets* **125**, e2019JE006111 (2020).

12. Fedorova, A. et al. Multi-annual monitoring of the water vapor vertical distribution on mars by spicam on mars express. *J. Geophys. Res.: Planets* **126**, e2020JE006616 (2021).
13. Montmessin, F. et al. Mars' water cycle and escape: a view from mars express and beyond. *Space Sci. Rev.* **220**, 77 (2024).
14. Aoki, S. et al. Global vertical distribution of water vapor on Mars: results from 3.5 years of ExoMars-TGO/NOMAD science operations. *J. Geophys. Res. Planets* **127**, e2022JE007231 (2022).
15. Fedorova, A. et al. A two-Martian years survey of the water vapor saturation state on Mars based on ACS NIR/TGO occultations. *J. Geophys. Res. Planets* **128**, e2022JE007348 (2023).
16. Whiteway, J. et al. Mars water-ice clouds and precipitation. *science* **325**, 68–70 (2009).
17. Villanueva, G. L. et al. The deuterium isotopic ratio of water released from the Martian caps as measured with TGO/NOMAD. *Geophys. Res. Lett.* **49**, e2022GL098161 (2022).
18. Brines, A. et al. Water vapor vertical distribution on Mars during perihelion season of MY 34 and MY 35 with ExoMars-TGO/NOMAD observations. *J. Geophys. Res. Planets* **128**, e2022JE007273 (2023).
19. Belyaev, D. A. et al. Revealing a high water abundance in the upper mesosphere of Mars with ACS onboard TGO. *Geophys. Res. Lett.* **48**, e2021GL093411 (2021).
20. Aoki, S. et al. Water vapor vertical profiles on Mars in dust storms observed by TGO/NOMAD. *J. Geophys. Res. Planets* **124**, 3482–3497 (2019).
21. Fedorova, A. A. et al. Stormy water on Mars: the distribution and saturation of atmospheric water during the dusty season. *Science* **367**, 297–300 (2020).
22. Kleinböhl, A. et al. Hydrogen escape on Mars dominated by water vapour photolysis above the hygropause. *Nat. Astron.* **8**, 827–837 (2024a).
23. Chaffin, M. S. et al. Martian water loss to space enhanced by regional dust storms. *Nat. Astron.* **5**, 1036–1042 (2021).
24. Vandaele, A. C. et al. Martian dust storm impact on atmospheric H2O and D/H observed by ExoMars Trace Gas Orbiter. *Nature* **568**, 521–525 (2019).
25. Brines, A. et al. Strong localized pumping of water vapor to high altitudes on Mars during the perihelion season. *Geophys. Res. Lett.* **51**, e2023GL107224 (2024).
26. Brines, A. et al. Water vapor vertical distribution on Mars after six years of TGO/NOMAD solar occultations. Part I: global climatology. *J. Geophys. Res. Planets (accepted May 2025)* (2025). https://doi.org/10.1029/2024JE008916.
27. Daerden, F. et al. Planet-wide ozone destruction in the middle atmosphere on Mars during global dust storm. *Geophys. Res. Lett.* **49**, e2022GL098821 (2022).
28. Navarro, T. et al. Global climate modeling of the Martian water cycle with improved microphysics and radiatively active water ice clouds. *J. Geophys. Res. Planets* **119**, 1479–1495 (2014).
29. Vals, M. et al. Improved modeling of mars' hdo cycle using a mars' global climate model. *J. Geophys. Res. Planets* **127**, e2022JE007192 (2022).
30. Rossi, L. et al. The hdo cycle on mars: comparison of acs observations with gcm simulations. *J. Geophys. Res. Planets* **127**, e2022JE007201 (2022).
31. Bhattacharyya, D., Clarke, J. T., Bertaux, J.-L., Chaufray, J.-Y. & Mayyasi, M. A strong seasonal dependence in the martian hydrogen exosphere. *Geophys. Res. Lett.* **42**, 8678–8685 (2015).
32. Bhattacharyya, D., Clarke, J., Bertaux, J.-L., Chaufray, J.-Y. & Mayyasi, M. Analysis and modeling of remote observations of the martian hydrogen exosphere. *Icarus* **281**, 264–280 (2017).
33. Chaffin, M. S. et al. Mars H escape rates derived from MAVEN/IUVS Lyman alpha brightness measurements and their dependence on model assumptions. *J. Geophys. Res. Planets* **123**, 2192–2210 (2018).
34. Zahnle, K., Haberle, R. M., Catling, D. C. & Kasting, J. F. Photochemical instability of the ancient martian atmosphere. *J. Geophys. Res.* Planets **113**, 3160 (2008).
35. Yelle, R. V. Diffusion limited escape of hydrogen from mars. *Icarus* **416**, 116099 (2024).
36. Mayyasi, M. et al. Solar cycle and seasonal variability of h in the upper atmosphere of mars. *Icarus* **393**, 115293 (2023).
37. Martín-Rubio, C., Vicente-Retortillo, A., Gómez, F. & Rodríguez-Manfredi, J. Interannual variability of regional dust storms between mars years 24 and 36. *Icarus* **412**, 115982 (2024).
38. Chaffin, M., Deighan, J., Schneider, N. & Stewart, A. Elevated atmospheric escape of atomic hydrogen from Mars induced by high-altitude water. *Nat. Geosci.* **10**, 174–178 (2017).
39. Neary, L. et al. Explanation for the increase in high-altitude water on Mars observed by NOMAD during the 2018 global dust storm. *Geophys. Res. Lett.* **47**, e2019GL084354 (2020).
40. Liuzzi, G. et al. Strong variability of Martian water ice clouds during dust storms revealed from ExoMars Trace Gas Orbiter/NOMAD. *J. Geophys. Res. Planets* **125**, e2019JE006250 (2020).
41. Luginin, M. et al. Properties of water ice and dust particles in the atmosphere of mars during the 2018 global dust storm as inferred from the atmospheric chemistry suite. *J. Geophys. Res.: Planets* **125**, e2020JE006419 (2020).
42. Stolzenbach, A. et al. Martian atmospheric aerosols composition and distribution retrievals during the first martian year of nomad/tgo solar occultation measurements: 1. methodology and application to the my 34 global dust storm. *J. Geophys. Res. Planets* **128**, e2022JE007276 (2023).
43. Sun, C., Yang, C., Li, T., Lai, D. & Fang, X. The atmospheric response to an unusual early-year Martian dust storm. *J. Geophys. Res. Planets* **130**, e2024JE008694 (2025).
44. Wang, H., Saidel, M., Richardson, M. I., Toigo, A. D. & Battalio, J. M. Martian dust storm distribution and annual cycle from Mars daily global map observations. *Icarus* **394**, 115416 (2023).
45. Smith, M. D. et al. First atmospheric science results from the Mars exploration rovers mini-TES. *Science* **306**, 1750–1753 (2004).
46. Montmessin, F., Forget, F., Rannou, P., Cabane, M. & Haberle, R. M. Origin and role of water ice clouds in the Martian water cycle as inferred from a general circulation model. *J. Geophys. Res. Planets* **109**, 2284 (2004).
47. Lemmon, M. et al. The Mars science laboratory record of optical depth measurements via solar imaging. *Icarus* **408**, 115821 (2024).
48. Smith, M. D. et al. Diurnal and seasonal variations of aerosol optical depth observed by MEDA/TIRS at Jezero crater, Mars. *J. Geophys. Res. Planets* **128**, e2022JE007560 (2023).
49. Smith, M. D. et al. The diurnal variation of dust and water ice aerosol optical depth at Jezero crater observed by MEDA/TIRS over a full Martian year. *Icarus* **425**, 116313 (2025).
50. Wang, H. & Fisher, J. A. North polar frontal clouds and dust storms on Mars during spring and summer. *Icarus* **204**, 103–113 (2009).
51. Cantor, B. A., James, P. B. & Calvin, W. M. MARCI and MOC observations of the atmosphere and surface cap in the north polar region of Mars. *Icarus* **208**, 61–81 (2010).
52. Daerden, F. et al. A solar escalator on Mars: self-lifting of dust layers by radiative heating. *Geophys. Res. Lett.* **42**, 7319–7326 (2015).
53. Cantor, B. A., James, P. B., Caplinger, M. & Wolff, M. J. Martian dust storms: 1999 Mars orbiter camera observations. *J. Geophys. Res. Planets* **106**, 23653–23687 (2001).
54. Määttänen, A. et al. A study of the properties of a local dust storm with Mars express OMEGA and PFS data. *Icarus* **201**, 504–516 (2009).
55. Spiga, A., Faure, J., Madeleine, J.-B., Määttänen, A. & Forget, F. Rocket dust storms and detached dust layers in the Martian atmosphere. *J. Geophys. Res. Planets* **118**, 746–767 (2013).

56. Heavens, N. G., Kass, D. M., Shirley, J. H., Piqueux, S. & Cantor, B. A. An observational overview of dusty deep convection in martian dust storms. *J. Atmos. Sci.* **76**, 3299–3326 (2019).
57. Daerden, F. et al. Mars atmospheric chemistry simulations with the GEM-Mars general circulation model. *Icarus* **326**, 197–224 (2019).
58. Montmessin, F. et al. Reappraising the production and transfer of hydrogen atoms from the middle to the upper atmosphere of mars at times of elevated water vapor. *J. Geophys. Res. Planets* **127**, e2022JE007217 (2022).
59. Holmes, J. et al. Enhanced water loss from the martian atmosphere during a regional-scale dust storm and implications for long-term water loss. *Earth Planet. Sci. Lett.* **571**, 117109 (2021).
60. Heavens, N. G. et al. Hydrogen escape from Mars enhanced by deep convection in dust storms. *Nat. Astron.* **2**, 126–132 (2018).
61. Chaffin, M. S. et al. Unexpected variability of Martian hydrogen escape. *Geophys. Res. Lett.* **41**, 314–320 (2014).
62. Newman, C. E., Lewis, S. R. & Read, P. L. The atmospheric circulation and dust activity in different orbital epochs on Mars. *Icarus* **174**, 135–160 (2005).
63. Gilli, G. et al. Increased hydrogen escape from Mars atmosphere during periods of high obliquity. *Nat. Astron* **9**, 960–968 (2025).
64. Stiller, G. P. The Karlsruhe Optimized and Precise Radiative transfer Algorithm (KOPRA). https://doi.org/10.5445/ir/270048971 (2000).
65. von Clarmann, V. et al. Retrieval of temperature and tangent altitude pointing from limb emission spectra recorded from space by the Michelson Interferometer for Passive Atmospheric Sounding (MIPAS). *J. Geophys. Res. Atmospheres* **108**, 3602 (2003).
66. Jurado Navarro, N. A. Retrieval of CO2 and collisional parameters from the MIPAS spectra in the earth atmosphere https://hdl.handle.net/10481/41725 (2016).
67. Brines, A. Water vapor distribution in the Martian atmosphere from solar occultation measurements by the spectrometer NOMAD / Trace Gas Orbiter https://hdl.handle.net/10481/97597 (2024).
68. Forget, F. et al. Improved general circulation models of the Martian atmosphere from the surface to above 80 km. *J. Geophys. Res. Planets* **104**, 24155–24175 (1999).
69. Lefèvre, F. et al. Relationship between the ozone and water vapor columns on Mars as observed by SPICAM and calculated by a global climate model. *J. Geophys. Res. Planets* **126**, e2021JE006838 (2021).
70. Holsclaw, G. M. et al. The Emirates Mars ultraviolet spectrometer (EMUS) for the EMM mission. *Space Sci. Rev.* **217**, 1–49 (2021).
71. Almatroushi, H. et al. Emirates Mars Mission characterization of Mars atmosphere dynamics and processes. *Space Sci. Rev.* **217**, 89 (2021).
72. Amiri, H. et al. The Emirates Mars Mission. *Space Sci. Rev.* **218**, 4 (2022).
73. Conrath, B. J. et al. Mars Global Surveyor Thermal Emission Spectrometer (TES) observations: atmospheric temperatures during aerobraking and science phasing. *J. Geophys. Res. Planets* **105**, 9509–9519 (2000).
74. Smith, M. D. et al. EMIRS observations of the aphelion-season Mars atmosphere. *Geophys. Res. Lett.* **49**, e2022GL099636 (2022).
75. Atwood, S. A. et al. Spatial and temporal variability of Martian water-ice cloud effective radius in EMIRS thermal infrared observations. *Icarus* **418**, 116148 (2024).
76. Wolff, M. J. et al. Constraints on dust aerosols from the Mars Exploration Rovers using MGS overflights and Mini-TES. *J. Geophys. Res. Planets* **111**, 2786 (2006).
77. Smith, M. D., Wolff, M. J., Clancy, R. T., Kleinböhl, A. & Murchie, S. L. Vertical distribution of dust and water ice aerosols from CRISM limb-geometry observations. *J. Geophys. Res. Planets* **118**, 321–334 (2013).
78. Willame, Y. et al. Retrieving cloud, dust and ozone abundances in the Martian atmosphere using SPICAM/UV nadir spectra. *Planet. Space Sci.* **142**, 9–25 (2017).
79. Spurr, R. J. D. Linearized radiative transfer theory: a general discrete ordinate approach to the calculation of radiances and analytic weighting functions, with application to atmospheric remote sensing. *Technische Universiteit Eindhoven* (TU/e, 2001).
80. Spurr, R. LIDORT and VLIDORT: linearized pseudo-spherical scalar and vector discrete ordinate radiative transfer models for use in remote sensing retrieval problems. *Light Scattering Reviews 3: Light Scattering and Reflection* 229–275 (Springer, 2008).
81. Rodgers, C. D. *Inverse Methods for Atmospheric Sounding: Theory and Practice*, vol. 2 (World Scientific, 2000).
82. Connour, K. et al. Another one derives the dust: ultraviolet dust aerosol properties retrieved from MAVEN/IUVS data. *Icarus* **387**, 115177 (2022).
83. Wolff, M. J. et al. Mapping water ice clouds on Mars with MRO/MARCI. *Icarus* **332**, 24–49 (2019).
84. Quémerais, E. et al. Stellar occultations observed by SPICAM on Mars Express. *J. Geophys. Res. Planets* **111**, 2604 (2006).
85. Trompet, L. et al. Carbon dioxide retrievals from NOMAD-SO on ESA's ExoMars Trace Gas Orbiter and temperature profile retrievals with the hydrostatic equilibrium equation: 2. Temperature variabilities in the mesosphere at Mars terminator. *J. Geophys. Res. Planets* **128**, e2022JE007279 (2023).
86. McCleese, D. et al. Mars climate sounder: an investigation of thermal and water vapor structure, dust and condensate distributions in the atmosphere, and energy balance of the polar regions. *J. Geophys. Res. Planets* **112**, 2790 (2007).
87. Kleinböhl, A. et al. Mars Climate Sounder limb profile retrieval of atmospheric temperature, pressure, and dust and water ice opacity. *J. Geophys. Res. Planets* **114**, 3358 (2009).
88. Kleinböhl, A. et al. Far infrared radiative properties of Mars atmospheric aerosols and their application to Mars Climate Sounder retrievals of aerosol profiles, aerosol columns and surface temperatures. *Icarus* **419**, 116000 (2024b).
89. Brines, A. et al. Out-of-season water escape during Mars' northern summer triggered by a strong localized dust storm [dataset] (2025).

Acknowledgements

AB and MLV acknowledges financial support from the Severo Ochoa grant CEX2021-001131-S and by grants PID2022-137579NB-100, RTI2018-100920-J-100 and PID2022-141216NB-100 all funded by MCIN/AEI/10.13039/501100011033. AB is suported by a JSPS Postdoctoral Fellowship for Research in Japan. SA is supported by JSPS KAKENHI Grant Number 24K21565, 22K03709, 22H05151, 22H00164, and 22KK0044. ExoMars is a space mission of the European Space Agency (ESA) and Roscosmos. The NOMAD experiment is led by the Royal Belgian Institute for Space Aeronomy (IASB-BIRA), assisted by Co-PI teams from Spain (IAA-CSIC), Italy (INAF-IAPS), and the United Kingdom (Open University). This project acknowledges funding by the Belgian Science Policy Office (BELSPO), with the financial and contractual coordination by the ESA Prodex Office (PEA 4000103401, 4000121493), by Spanish Ministry of Science and Innovation (MCIU) and by European funds under grant PGC2018-101836-B-100, as well as by UK Space Agency through grants ST/V002295/1, ST/V005332/1, ST/Y000234/1 and ST/X006549/1 and Italian Space Agency through grant 2018-2-HH.0. This project has received funding from the European Union's Horizon 2020 research and innovation program under grant agreement No 101004052. This work was supported by the Belgian Fonds de la Recherche Scientifique - FNRS (grant 30442502; ET-HOME). US investigators were supported by the National Aeronautics and Space Administration. GLV and MDS were supported by NASA's Mars Program Office under the "GSFC participation in the TGO/NOMAD Investigation of Trace Gases on Mars" agreement. This work is supported by NASA under award number 80GSFC24M0006. Work at the Jet Propulsion Laboratory, California Institute of Technology, is performed under contract with the National Aeronautics and Space Administration (80NM0018D0004). Funding for development of the EMM mission was provided by the UAE

government, and to co-authors outside of the UAE by MBRSC and the UAE Space Agency. Canadian investigators were supported by the Canadian Space Agency.

Author contributions

A.B., S.A., and F.D. led the study, analyzed the main results, and led the writing of the paper. A.B. and S.A. contributed to the processing of NOMAD/SO data. S.A. contributed to the processing of MRO/MCS data. F.D. contributed to the interpretation of MRO/MCS data. M.S.C. contributed to the processing of EMM/EMUS data and the discussion of the paper. S.A.A. and S.R. contributed to the processing of EMM/EMIRS data and the discussion of the paper. B.A.C. contributed to the analysis of MRO/MARCI images and the discussion of the paper. Y.W. contributed to the processing of NOMAD/UVIS data. L.T. contributed to the processing of NOMAD/SO data. G.L.V., M.J.W., M.D.S., and C.S.E. contributed to the discussion of the paper. I.R.T. contributed to the calibration of the NOMAD data and the discussion of the paper. G.L., L.N., and M.R.P. contributed to the discussion of the paper. M.Á.L.-V. contributed to the editing and discussion of the paper. A.K. contributed to the processing of MRO/MCS data and to the editing and discussion of the paper. H.A. contributed to the processing of EMM data. J.W. contributed to the discussion of the paper. A.C.V., B.R., and G.B. contributed to the acquisition of NOMAD data.

Competing interests

The authors declare no competing interests.

Additional information

Supplementary information The online version contains supplementary material available at https://doi.org/10.1038/s43247-025-03157-5.

Correspondence and requests for materials should be addressed to Adrián. Brines or Shohei Aoki.

Peer review information *Communications Earth & Environment* thanks the anonymous, reviewer(s) for their contribution to the peer review of this work. Primary Handling Editor: Joe Aslin. [A peer review file is available].